Review of
Scientific Instruments

RESEARCH ARTICLE | MAY 04 2026

Correlative *in situ* x-ray photoelectron spectroscopy and transmission electron microscopy characterization under identical reaction conditions

Jun Cai ; Zhuoran Yao ; Yijing Zang ; Yulu He ; Yang Gu ; Kaihui Liu ; Zhi Liu ;
Zhu-Jun Wang

Rev. Sci. Instrum. 97, 055202 (2026)
https://doi.org/10.1063/5.0308362

AIP Publishing

Review of
Scientific Instruments

ARTICLE

pubs.aip.org/aip/rsi

Correlative *in situ* x-ray photoelectron spectroscopy and transmission electron microscopy characterization under identical reaction conditions

Cite as: Rev. Sci. Instrum. 97, 055202 (2026); doi: 10.1063/5.0308362
Submitted: 21 October 2025 • Accepted: 10 April 2026 •
Published Online: 4 May 2026

Jun Cai,[1,2,3] Zhuoran Yao,[1] Yijing Zang,[2] Yulu He,[1] Yang Gu,[1,2] Kaihui Liu,[4]
Zhi Liu,[1,2] and Zhu-Jun Wang[1,2,a)]

AFFILIATIONS

[1] School of Physical Science and Technology, ShanghaiTech University, Shanghai 201210, China
[2] Center for Transformative Science, ShanghaiTech University, Shanghai 201210, China
[3] Shanghai Synchrotron Radiation Facility Shanghai Advanced Research Institute, Chinese Academy of Sciences, Shanghai 20124, China
[4] State Key Laboratory for Mesoscopic Physics, Frontiers Science Centre for Nano-optoelectronics, School of Physics, Peking University, Beijing 100871, China

[a)] **Author to whom correspondence should be addressed:** wangzhj3@shanghaitech.edu.cn

ABSTRACT

Acquiring information on the evolution of chemical states and real-space morphological changes under identical reaction conditions is crucial for elucidating the mechanisms of heterogeneous catalytic reactions. In this study, we design and implement a microreactor with high electron transparency, enabling correlated *in situ* x-ray photoelectron spectroscopy (XPS) and transmission electron microscopy (TEM) measurements for the same type of sample under identical reaction environments, while integrating online mass spectrometry for seamless coupling of spectroscopic and imaging data. This advancement allows direct correlation between the *in situ* chemical-state information obtained by XPS and the real-space structural evolution captured by TEM. Using the oxidation–reduction process of Ni nanoparticles in O_2/H_2 atmospheres as a model reaction, we systematically investigate the dynamic relationship between surface chemical states and morphological reconstruction from near-ambient to ambient pressures, demonstrating the stability and applicability of the microreactor under complex gas environments. This work provides a new experimental approach for mechanistic studies of gas–solid interfacial reactions under realistic operating conditions and establishes a methodological foundation for the rational design and optimization of high-performance catalysts.

I. INTRODUCTION

Understanding the mechanism of interfacial catalytic reactions requires the acquisition of information on the evolution of surface chemical states and morphological structures of catalysts under realistic reaction conditions.[1–3] Combining *in situ* chemical-state analysis with *in situ* structural characterization, the dynamic behavior of active species and their structure–performance relationships can be elucidated.[4–6] Such correlative studies are essential for gaining fundamental insights into heterogeneous catalysis, improving reaction selectivity and catalytic efficiency, and enabling the rational design of high-performance catalysts.[7,8]

To achieve these goals, ambient-pressure x-ray photoelectron spectroscopy (AP-XPS) and *in situ* transmission electron microscopy (*in situ* TEM) have emerged as two powerful yet complementary techniques for probing catalytic reaction mechanisms at gas–solid interfaces.[9–13] AP-XPS enables the identification of surface chemical states and adsorbed species within the near-surface region (on the nanometer scale) under reactive gas atmospheres, such as revealing distinct adsorption configurations and key intermediates during small-molecule reactions on metal catalysts.[14,15] In contrast, *in situ* TEM allows direct observation of morphological and crystallographic evolution at the atomic scale under near-ambient to ambient pressures, providing critical information on structural reconstruction and phase transformations during reactions.[16,17]

However, due to limitations in instrument design and window materials, the working pressure of conventional AP-XPS typically does not exceed ~25 mbar, preventing true ambient-pressure measurements. Although *in situ* TEM can operate at higher pressures,[18] the commonly used Si_3N_4 chip windows are opaque to low-energy photoelectrons (<1000 eV),[19,20] making them incompatible with XPS measurements. Consequently, these two *in situ* techniques differ significantly in key experimental parameters, such as pressure, gas composition, temperature, and gas hourly space velocity (GHSV)—a discrepancy often referred to as the "pressure/conditions gap." The inability to acquire spectroscopic and imaging data under identical conditions precludes direct correlation between real-space structural evolution and electronic-state changes, thus hindering accurate elucidation of the dynamic behavior of active sites and their structure–activity relationships under realistic operating environments.

To bridge this gap, it is imperative to develop a characterization platform capable of performing *in situ* XPS and TEM under fully identical reaction conditions, with real-time control of pressure, temperature, gas composition, and GHSV. Although several reaction cells and methods designed for AP-XPS, such as the de Laval nozzle,[21] "virtual cell,"[22] and graphene reaction cell,[23,24] have improved pressure tolerance,[21,23–27] they are generally incompatible with TEM imaging. Conversely, conventional *in situ* TEM chips are suitable for electron-beam imaging but fail to meet the transparency requirements for photoelectron detection.[20,28,29] Therefore, the establishment of a unified methodology that enables same-cell, same-condition, multimodal characterization represents a crucial step toward bridging the long-standing divide between spectroscopy and microscopy.

In this work, we propose and construct a microreactor based on multilayer single-crystalline graphene windows. Graphene possesses excellent electron transparency and gas impermeability, while its multilayer structure provides the necessary mechanical strength to withstand ambient-pressure operation.[30–32] This design allows correlated *in situ* TEM and XPS measurements for the same type of sample to be performed within the same reaction cell and under identical experimental conditions. The microreactor supports pressures up to 1 bar, enabling true ambient-pressure XPS–TEM correlative studies. Integrated with a microfluidic flow-control system, the platform offers precise and reproducible control over GHSV and residence time, along with real-time monitoring and calibration of temperature and gas composition throughout the experiment. With this configuration, surface chemical-state and adsorbate information obtained from XPS can be directly correlated with the morphological and crystallographic evolution captured by TEM for the same type of sample, enabling the reconstruction of catalytic dynamics under realistic working conditions. Furthermore, the temporal resolution can reach 0.1 s for both *in situ* XPS and TEM measurements, while the spatial resolution for ambient-pressure TEM characterization can reach 0.07 nm.

Using the oxidation–reduction of Ni nanoparticles in O_2 and H_2 environments as a model system, we systematically investigate the coupling between valence-state evolution and morphological reconstruction across pressures ranging from near-ambient to ambient conditions. The results validate the reliability, stability, and general applicability of this correlative approach for elucidating structure–performance relationships in catalysis. The main contributions of this study are as follows: (i) development of a same-cell, same-condition platform enabling correlated *in situ* XPS and TEM for the same type of sample at ambient pressure; (ii) realization of precise and reproducible control over pressure, temperature and GHSV through microfluidic regulation; AND (iii) establishment of a data-alignment and experimental-calibration protocol that minimizes uncertainties in cross-technique comparison.

II. INSTRUMENTATION

A. Design of the multilayer single-crystalline graphene microreactor

Figure 1 presents the structural schematic of the multilayer single-crystalline graphene microreactor. The overall assembly consists of a functional chip, a window chip, sealing O-rings, a supporting base, and fixing screws [Figs. 1(a) and 1(b)]. A narrow gap of ~10 μm is formed between the functional chip and the window chip, serving as the effective reaction zone of the microreactor. The graphene used in this work is grown by isothermal carbon diffusion through single crystal nickel foil (note 1 in the supplementary material) and is subsequently transferred onto the target chip/window substrate.

The functional chip integrates four heating electrodes and four thermocouple electrodes that are used for sample heating and temperature monitoring, enabling high-precision Proportion Integration Differentiation (PID) temperature control. In addition, the functional chip is connected to a microfluidic system that provides separate gas inlet and outlet channels, thus forming a controllable gas-flow circuit. This configuration allows the internal atmosphere of the reaction cell to be precisely coupled with the external gas-supply system, enabling accurate control of the gas composition, pressure, and GHSV.

When employed for *in situ* TEM observations, the microreactor is mounted on a dedicated TEM gas-cell holder, as shown in Fig. 1(c). For *in situ* XPS measurements, the same microreactor used in TEM experiments can be directly installed at the front end of a custom-designed XPS sample holder [Fig. 1(d)], thereby enabling correlative tracking of the same sample under identical reaction conditions. The heating and thermocouple electrodes are connected to the external circuit through a custom vacuum-flange LEMO interface, while the gas inlet and outlet channels are coupled to the external gas-supply system via vacuum feedthrough connectors.

The TEM measurements were performed on a JEOL Cs-corrected TEM (JEM-ARM 300F, GRAND ARM). The XPS experiments were carried out on a lab-based AP-XPS system, equipped with a PHOIBOS 150 NAP analyzer and a μ-FOCUS 600 x-ray source, with an angle of 55° between the analyzer axis and the x-ray incident direction.[12] This microreactor is also compatible with the synchrotron-based near-atmospheric photoelectron spectroscopy system we developed.[33]

In TEM operation, the microreactor is positioned between the upper and lower pole pieces of the microscope, allowing the electron beam to pass through the reaction cell for real-space imaging

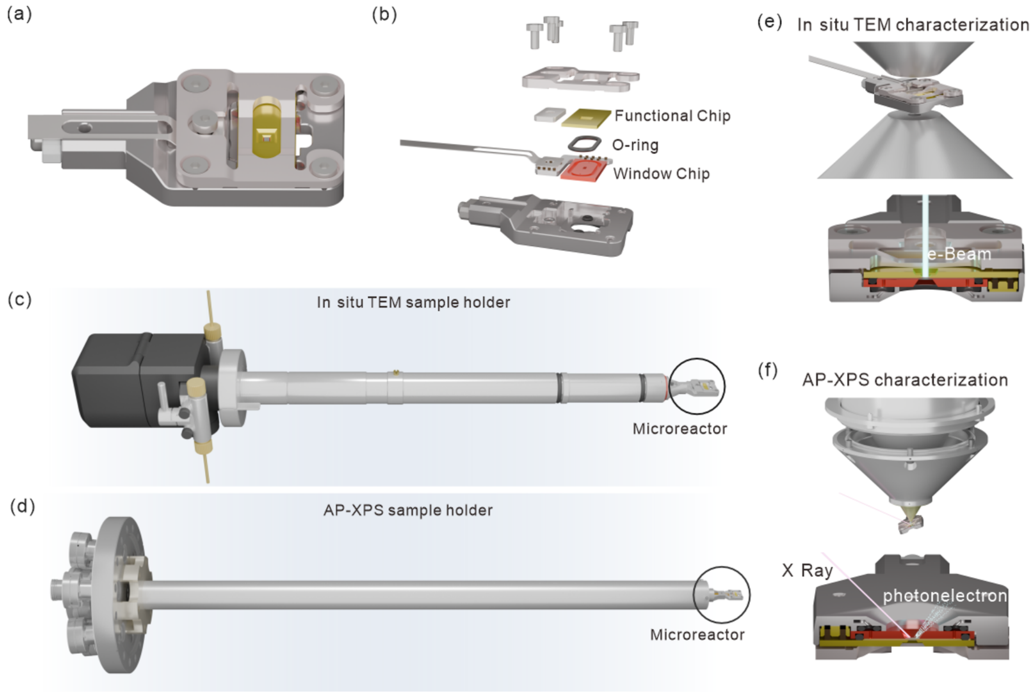

FIG. 1. Design of the microreactor used in XPS and TEM characterization. (a) Schematic diagrams of the microreactor; (b) exploded view of the microreactor; (c) *in situ* TEM sample holder and (d) AP-XPS sample holder; the black circle in [(c) and (d)] was the microreactor; [(e) and (f)] microreactor used in *in situ* TEM characterization and AP-XPS characterization, respectively.

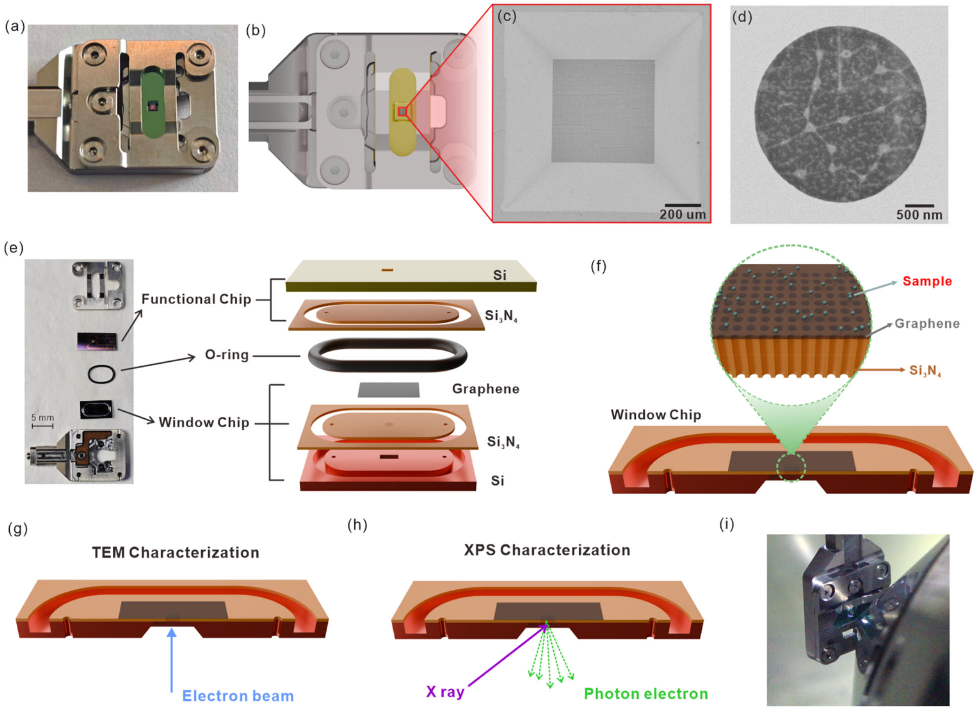

FIG. 2. Detailed structure of the microreactor. (a) Image of the microreactor; (b) top view of the microreactor; [(c) and (d)] SEM images of the graphene-covered Si_3N_4 window; (e) exploded view of the functional chip and window chip; (f) illustration of the sample on the window chip, showing the sample deposited on the graphene; (g) illustrations of electron beam interaction with the microreactor; (h) illustration of x-ray interaction with the microreactor; (i) photograph of the microreactor during XPS experiment.

[Fig. 1(e)]. In the XPS mode, x rays penetrate the window region of the microreactor to excite photoelectrons from the sample surface, which are then collected by the analyzer to obtain information on the surface chemical states of the sample [Fig. 1(f)].

The differences between TEM and XPS configurations are primarily in the external interfaces/adapters (to couple to the TEM holder vs the XPS sample stage), whereas the microreactor body [black circle in Figs. 1(c) and 1(d), chip stack, graphene window, sealing concept, gas flow path, and reaction volume] remains the same.

Figure 2 shows the internal structure and sample-loading configuration of the microreactor. Figures 2(a) and 2(b) present the image and overall top view of the microreactor, while Fig. 2(e) displays an exploded structural schematic. Unlike conventional *in situ* TEM chips, the window chip in this design adopts a three-layer configuration consisting of a Si substrate, a Si_3N_4 supporting membrane, and a graphene thin film. Figures 2(c) and 2(d) show Scanning Electron Microscopy (SEM) images of the window region, where the gray area corresponds to a porous Si_3N_4 membrane ∼100 nm thick with pore diameters of about 6 μm. The surface of this membrane is coated with multilayer single-crystalline graphene films [Fig. 2(d)]. The sample was deposited by drop-casting onto the graphene film of the window chip, as shown in Fig. 2(f). Figure 2(g) illustrates the interaction of the electron beam with the microreactor in the *in situ* TEM characterization, while Fig. 2(h) illustrates the interaction of the x-ray with the microreactor and the photon electrons emitted from the sample. The photograph of the microreactor in the XPS chamber is shown in Fig. 2(i).

This multilayer graphene–Si_3N_4 composite structure provides both mechanical robustness and high optical/electron transparency, combining the advantages of both materials: (i) The Si_3N_4 supporting framework ensures mechanical stability and allows transmission of high-energy electrons and x rays, although it is opaque to low-energy photoelectrons (below 1000 eV);[20] (ii) the multilayer single-crystalline graphene film is atomically thin, highly transparent to electrons and photoelectrons, and effectively gas-impermeable, enabling the transmission of low-energy photoelectrons and, thus, ensuring the feasibility of XPS measurements;[20] (iii) the multilayer stacking significantly enhances the mechanical strength while maintaining excellent transparency, allowing the microreactor to withstand gas pressures approaching 1.2 bars.

The catalyst samples are loaded onto the surface of the graphene/Si_3N_4 supporting framework, where the graphene coverage exceeds 30% [Fig. 2(e)], ensuring an optimal balance between signal intensity and transmission efficiency for both TEM imaging and XPS detection. This structural design serves as the core foundation for achieving correlated *in situ* XPS and TEM measurements under identical reaction conditions within the same microreactor.

B. Gas handling system

Figure 3 illustrates the schematic of the gas-supply system for the microreactor. Figures 3(a) and 3(b) show the photograph and the structural model of the system, while Fig. 3(c) presents the logical flow diagram. The system is composed of mass flow controllers, diaphragm valves, a pressure regulator, a molecular pump, a mechanical pump, a wide-range pressure gauge, and an online quadrupole mass spectrometer [QMS, labeled as “iii” in Fig. 3(c)].

The gas flow is first adjusted by the flow controllers and pressure regulators before entering the reaction cell, where the pressure stabilizer ensures precise control of the chamber pressure. The gas in and gas out were labeled as “i” and “ii” in Fig. 3(c). When the pressure exceeds the preset value, excess gas is automatically vented through a bypass outlet. On the exhaust side [labeled as “iv” in Fig. 3(c)], a flow sensor monitors the actual flow rate of the inlet gas, and the online mass spectrometer continuously monitors and analyzes the composition of the reaction atmosphere in real time.

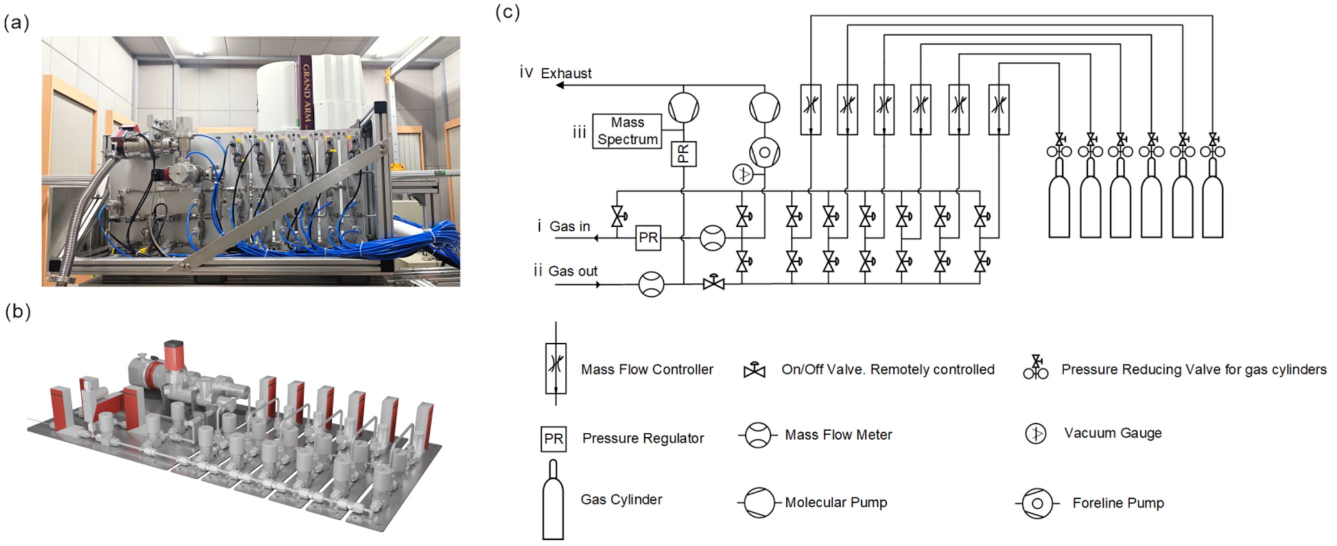

FIG. 3. Gas supply system. (a) Image and (b) drawing of the gas handling system; (c) logic diagram of the gas handling system.

C. Temperature and pressure control of the microreactor

To evaluate the pressure-control performance of the system, tests were conducted under a 20% O_2 + 80% Ar atmosphere. As shown in Fig. 4(a), the system maintains stable and precise pressure control up to a maximum operating pressure of 1.2 bars, while the mass spectrometer accurately reflects real-time changes in the gas composition inside the reactor [Fig. 4(b)]. Furthermore, stability tests were carried out under both reducing (H_2) and oxidizing (O_2) atmospheres at different temperatures. Under 1 bar of 10% H_2 + 90% Ar, the microreactor remained stable up to 800 °C [Fig. 4(c)], with the graphene window fully intact. Under 1 bar of 20% O_2 + 80% Ar, the system maintained stable operation up to 350 °C, with a temperature fluctuation of less than ±0.1 °C [Fig. 4(d)].

Based on our tests, the microreactor remains stable up to 800 °C under 1 bar of 10% H_2 + 90% Ar. Under oxidizing conditions (e.g., 1 bar of 20% O_2 + 80% Ar), the maximum operating temperature is 350 °C, primarily limited by the oxidation susceptibility of the multilayer graphene window at elevated temperatures.[34] In addition, at 300 K, the microreactor supports stable pressure control up to 1.2 bars.

These results demonstrate that the graphene-based microreactor exhibits excellent gas tightness and thermal stability over a wide temperature range and under various complex gaseous environments, providing a reliable platform for *in situ* characterization under realistic reaction conditions.

III. EXPERIMENTAL RESULTS

To further evaluate the applicability of the microreactor under realistic reaction environments, the oxidation–reduction process of Ni nanoparticles was selected as a model catalytic system. Using this setup, both the chemical-state evolution and the morphological/structural transformation of Ni nanoparticles could be monitored under identical reaction conditions, enabling direct correlation between spectroscopic and imaging information.

Figure 5(a) shows the Ni 2p spectra under oxygen conditions at 500 K. The peak at 852.6 and 855 eV was contributed to the metallic nickel and nickel oxide, respectively.[35,36] During oxidation, the Ni 2p spectra reveal progressive oxidation with increasing O_2 partial pressure: partial oxidation is observed at 1 mbar O_2 and 500 K, and complete conversion to Ni oxide occurs at 1 bar O_2.

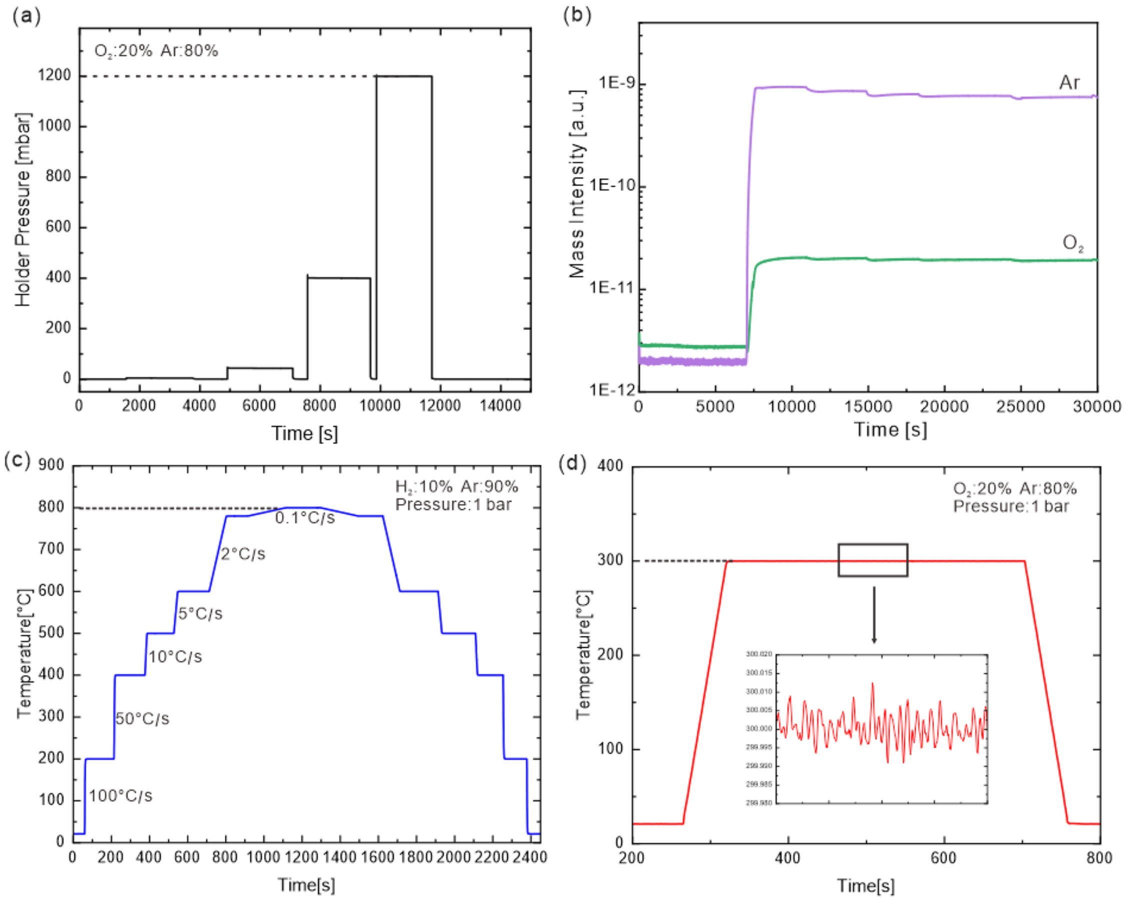

FIG. 4. Sample temperature and pressure control of the microreactor. (a) Staged temperature rise curve with different increasing rate; (b) stability of the temperature control; (c) pressure control in the microreactor from mbar level to atmosphere pressure; (d) mass intensity of the gas in the microreactor.

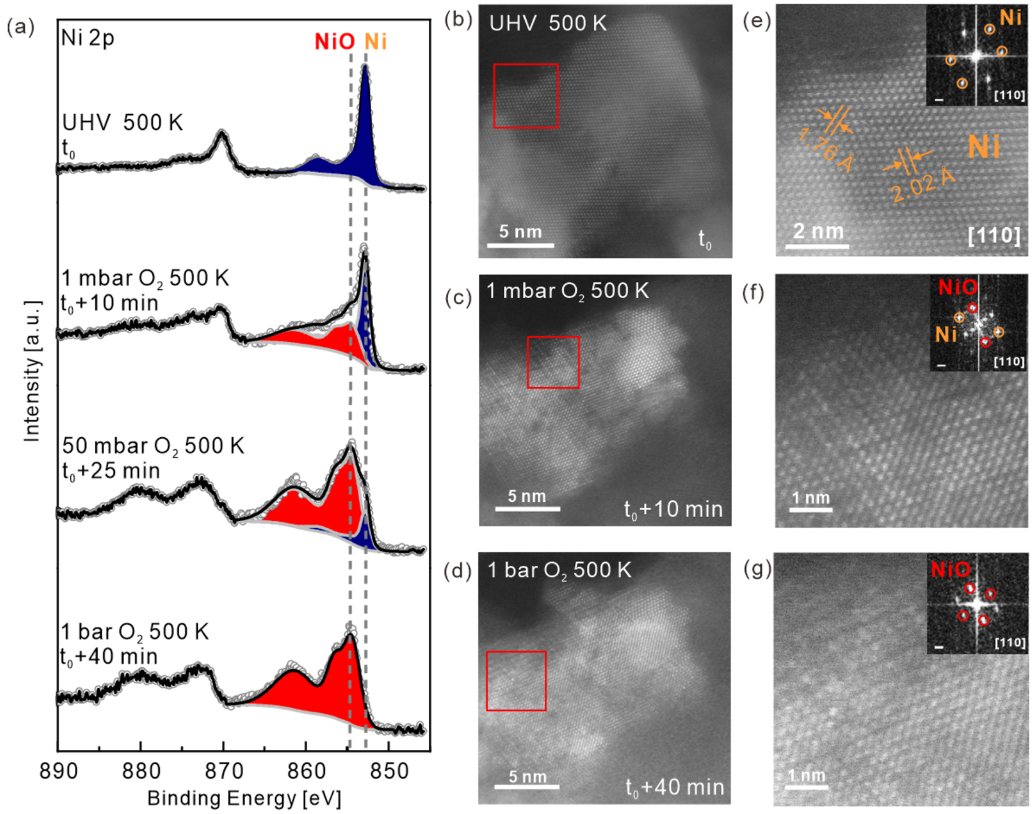

FIG. 5. AP-XPS and *in situ* high resolution TEM characterization of Ni nanoparticles during the O_2 oxidation process. (a) Ni 2p spectra of the Ni nanoparticle at 500 K, with oxygen pressure increasing from 1 mbar to 1 bar; [(b)–(d)] *In situ* TEM images of the Ni nanoparticle during the oxidation process; [(e)–(g)] enlarged images and corresponding diffractograms for [(b) and (e)], [(c) and (f)], and [(d) and (g)], illustrating the transition from metallic Ni to NiO during oxidation; the scale bar in the FFT patterns is 2 nm^{-1}.

Figures 5(b)–5(d) show the *in situ* high resolution TEM (HRTEM) images of the Ni nanoparticles. Figures 5(e)–5(g) show the atomic structure of the red square box region in Figs. 5(b)–5(d), respectively. The insets display fast Fourier transform diffractograms of the HRTEM images in Figs. 5(e)–5(g). Compared with the previously studies on nickel oxidation and reduction,[35,37–39] our results also reveal a clear transition from metallic Ni to Ni oxide, in agreement with the spectroscopic data. This direct correspondence between the chemical-state evolution and structural transformation at different oxidation stages confirms the synchronized dynamic behavior of Ni nanoparticles.

Subsequently, the reduction process of fully oxidized NiO was investigated under a hydrogen atmosphere. The reduction of Ni oxide was characterized by AP-XPS and *in situ* HRTEM, as shown in Figs. 6(a)–6(d). The Ni 2p spectra in Fig. 6(a) exhibit a gradual shift toward lower binding energies, indicating the stepwise reduction of Ni oxide to metallic Ni as the H_2 pressure and temperature increase. Complete reduction of Ni oxide was occurred at 1 bar H_2 and 700 K. The *in situ* HRTEM images during the reduction process are shown in Figs. 6(b)–6(d). Figures 6(e)–6(g) show the atomic structure of the red square box region in Figs. 6(b)–6(d), respectively. The insets in Figs. 6(e)–6(g) display fast Fourier transform diffractograms of the HRTEM images, which confirm the re-emergence of metallic Ni nanoparticles. The quantitative analysis of the XPS spectra and HRTEM images during oxidation and reduction reaction provides a dynamic profile of the Ni/Ni oxide ratio during the entire redox cycle, as shown in note 3 of the supplementary material and Fig. 7. The structural evolution observed via TEM is in excellent agreement with the chemical state transitions captured by XPS, thereby providing a more comprehensive understanding of the surface-interface dynamics. It should be noted that the *in situ* HRTEM and XPS data were collected on the different spots:

A. *In situ* HRTEM characterization

(i) Oxidation process: HRTEM data were collected continuously from the same reaction region/same field of view to ensure consistency and comparability between structural evolution. (ii) Reduction process: Since the transition from oxidation to reduction requires switching gases and performing cooling/reheating operations, the overall state of the sample changes, accompanied by inevitable drift and repositioning. Therefore, for the reduction process in the HRTEM characterization, we selected a different field of view (choosing a representative particle from the overall oxidized Ni

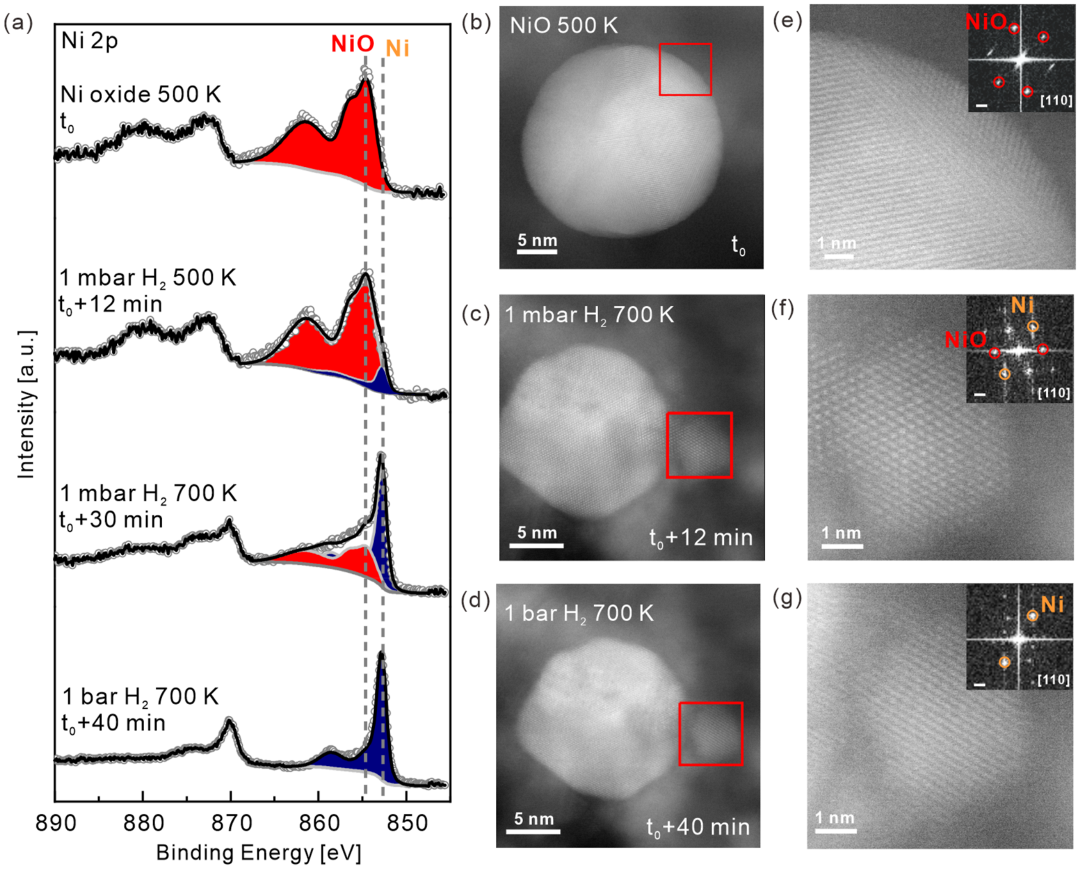

FIG. 6. AP-XPS and *in situ* HRTEM characterization of NiO nanoparticles during the H_2 reduction process. (a) Ni 2p spectra of the nanoparticles with H_2 pressure increasing from 1 mbar to 1 bar; [(b)–(d)] in situ TEM images of Ni/NiO nanoparticles during the reduction process; [(e)–(g)] Enlarged images and corresponding diffractograms for [(b) and (e)], [(c) and (f)], and [(d) and (g)], showing the transition from NiO to metallic Ni during the reduction process, scale bar in the FFT patterns: 2 nm^{-1}.

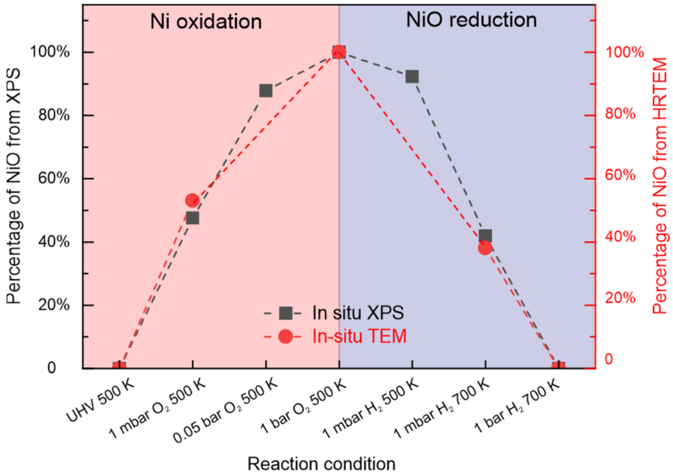

FIG. 7. Evolution of the NiO percentage during oxygen oxidation and hydrogen reduction process.

region) to capture the reduction process. This is why the fields of view in the oxidation and reduction stages of Fig. 5 appear different.

B. *In situ* XPS characterization

During *in situ* XPS characterization of oxidation or reduction processes, since XPS provides averaged chemical state information from the x-ray illuminated region of the sample, it is not affected by changes in the sample's position.

Because the temperature, pressure, gas composition, and flow rate remained identical during both XPS and TEM experiments, the spectroscopic and imaging results could be precisely correlated. This enabled a direct and accurate elucidation of the dynamic structural and chemical-state evolution of Ni nanoparticles during oxidation and reduction. These findings not only verify the stability and practicality of the microreactor but also demonstrate its unique capability to bridge the experimental gap between XPS and TEM under consistent reaction conditions.

The system provides both high spatial resolution imaging and fast spectroscopic acquisition. *In situ* HRTEM system delivers a spatial resolution of 0.06 nm under vacuum. Under ambient-pressure conditions, the attainable resolution is mainly governed by electron-beam scattering in the window and gas;[29,40] the microreactor employs an ultrathin 1–2 nm multilayer graphene window supported on a porous Si_3N_4, which substantially reduces scattering compared with conventional ~50 nm Si_3N_4 membranes,[41] enabling high-resolution imaging of 0.07 nm under 1 bar (10% H_2 + 90% Ar) (note 2 in the supplementary material). In addition, using graphene can also reduce silicon contamination during *in situ* TEM experiments compared to using a Si_3N_4 chip.[42]

The temporal resolution could reach 0.1 s for both the rapid XPS acquisition and the fastest TEM imaging, allowing correlated tracking of morphology and chemical-state dynamics on sub-second timescales. The details about the spatial and temporal resolution are shown in note 2 of the supplementary material .

Overall, the designed graphene microreactor enables correlated *in situ* XPS and TEM characterization under fully identical reaction conditions. With the integration of an online QMS system, data obtained from both techniques can be synchronously and dynamically correlated, allowing the establishment of a direct mapping between chemical-state changes and structural evolution.

The successful development of this system demonstrates the feasibility of simultaneous *in situ* XPS and TEM data acquisition under realistic reaction environments. As illustrated in Fig. 8, an integrated gas-delivery and exhaust-analysis concept intended to ensure that the two platforms can be operated under identical reaction conditions, and it also provides the capability to distribute the same premixed gas to both the XPS and TEM setups in parallel. In operation, the gas mixture from the supply unit is combined in a mixing chamber and then split into two parallel branches: one branch feeds the XPS side microreactor, and the other feeds the TEM-side microreactor. Both branches form closed flow paths of "gas inlet → microreactor → gas outlet." To minimize differences in gas switching and delivery timing, the effective line lengths of the two branches were designed to be as closely matched as possible. The mass spectrometer (MS) is placed at the outlet side for online analysis of reaction products: the two outlet branches merge downstream and are connected to a single MS inlet, enabling product monitoring. This configuration allows true synchronous characterization of

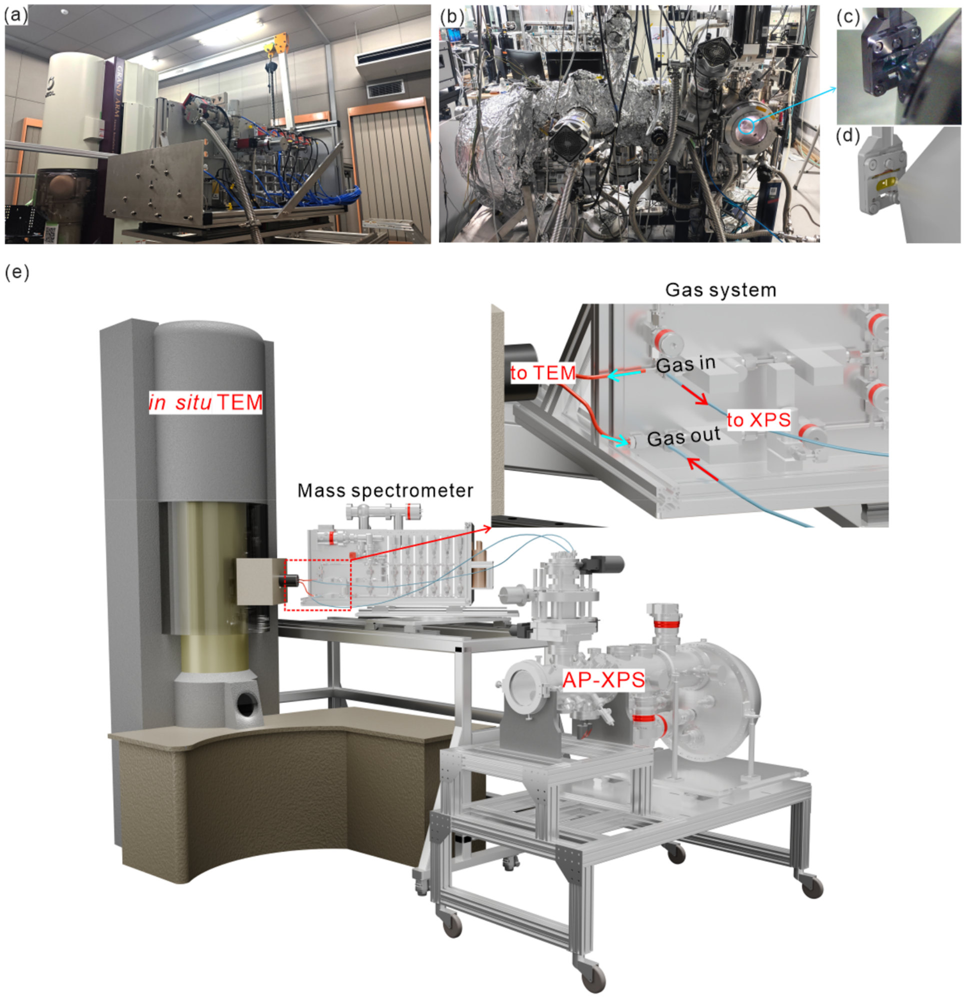

FIG. 8. Schematic illustration of the integrated *in situ* XPS–TEM system. (a) Image of the *in situ* TEM and gas supply system; (b) photograph of the AP-XPS setup; (c) photograph and (d) schematic of the microreactor in the AP-XPS chamber; (e) schematic of the integrated *in situ* XPS-TEM system.

the same sample under identical gas composition and temperature, ensuring complete consistency of experimental conditions across both techniques.

Through this design, the chemical-state information (from XPS) and the morphological/structural information (from TEM) can be acquired in real time on a synchronized reaction conditions, achieving precise temporal coupling and cross-validation between spectroscopic and imaging signals. This approach provides a powerful experimental platform for multidimensional dynamic analysis of non-equilibrium reaction processes at gas–solid interfaces.

IV. CONCLUSION

In this work, we designed a multilayer single-crystalline graphene microreactor, achieving correlated *in situ* XPS and TEM characterization of the same type of sample under the same conditions. This design shows a reproducible correlative *in situ* XPS–TEM capability at true ambient pressure using the same reactor and identical reaction conditions. By directly correlating spectroscopic information (chemical states, adsorbed species) with imaging information (morphology, structural evolution) under identical pressure, temperature, and gas-flow conditions, this platform effectively eliminates the "pressure/conditions gap" between XPS and TEM.

This methodological innovation ensures the comparability and reproducibility of results obtained from different *in situ* techniques and provides a powerful new tool for investigating the true reaction mechanisms of catalysts under industrially relevant conditions. Using this approach, the dynamic evolution of catalysts during reactions can be captured with higher accuracy, offering essential insights for the optimization and rational design of catalytic materials. In the future, this graphene-based microreactor is expected to use in heterogeneous catalysis, energy conversion, and interfacial science, advancing mechanistic studies toward more realistic, industry-relevant environments.

SUPPLEMENTARY MATERIAL

Note 1 in the supplementary material shows the growth method of the multilayer graphene. Note 2 shows the temporal and spatial resolution of the system. Note 3 shows the quantity analysis of the HRTEM images.

ACKNOWLEDGMENTS

This work was mainly supported by the National Natural Science Foundation of China under Grant No. T2525029. The authors acknowledge DENS solutions for their help and assistance during the design. This work was supported by the National Key R&D Program of China under Grant No. 2022YFA1503802 and the National Natural Science Foundation of China under Grant Nos. 22572122, T2450058, 22502123, 12027804 and 22002090. The authors thank the Shanghai Synchrotron Radiation Facility of BL02B01 (31124.02.SSRF.BL02B01) for the assistance on *in situ* XPS measurements.

AUTHOR DECLARATIONS

Conflict of Interest

The authors have no conflicts to disclose.

Author Contributions

J.C. conceived the research and supervised the project. J.C. designed the microreactor. The experiments were performed by Z.Y., Y.Z., Y.H., Y.G., and J.C. Important contributions to the interpretation of the results and conception and writing of the manuscript were made by J.C. and Z.-J.W. All authors participated in the scientific discussion.

Jun Cai: Conceptualization (lead); Data curation (equal); Formal analysis (lead); Funding acquisition (lead); Investigation (lead); Methodology (equal); Project administration (equal); Supervision (lead); Writing – original draft (lead); Writing – review & editing (equal). **Zhuoran Yao**: Data curation (equal); Writing – original draft (lead). **Yijing Zang**: Data curation (equal); Formal analysis (equal); Writing – original draft (equal). **Yulu He**: Data curation (equal); Formal analysis (equal). **Yang Gu**: Data curation (equal); Formal analysis (equal). **Kaihui Liu**: Resources (equal); Supervision (equal). **Zhi Liu**: Funding acquisition (equal); Project administration (equal); Resources (equal); Supervision (equal). **Zhu-Jun Wang**: Conceptualization (equal); Funding acquisition (lead); Project administration (equal); Resources (lead); Supervision (lead); Writing – review & editing (equal).

DATA AVAILABILITY

The data that support the findings of this study are available from the corresponding author upon reasonable request.

REFERENCES

[1] G. A. Somorjai and Y. Li, *Introduction to Surface Chemistry and Catalysis* (John Wiley & Sons, 2010).

[2] J. R. Ross, *Heterogeneous Catalysis: Fundamentals and Applications* (Elsevier, 2011).

[3] H. E. G. K, F. Schueth, and J. Weitkamp, *Handbook of Heterogeneous Catalysis 1–8* (Wiley, 2008).

[4] M. A. Bañares and M. Daturi, Catal. Today **423**, 114255 (2023).

[5] A. M. Beale, S. D. M. Jacques, and B. M. Weckhuysen, Chem. Soc. Rev. **39**(12), 4656–4672 (2010).

[6] J. Cai, L. Wei, J. Liu, C. Xue, Z. Chen, Y. Hu, Y. Zang, M. Wang, W. Shi, T. Qin, H. Zhang, L. Chen, X. Liu, M.-G. Willinger, P. Hu, K. Liu, B. Yang, Z. Liu, Z. Liu, and Z.-J. Wang, Nat. Mater. **23**(12), 1654–1663 (2024).

[7] L. Liu and A. Corma, Nat. Rev. Chem. **5**(4), 256–276 (2021).

[8] J. Kim, H. Choi, D. Kim, and J. Y. Park, ACS Catal. **11**(14), 8645–8677 (2021).

[9] D. E. Starr, Z. Liu, M. Hävecker, A. Knop-Gericke, and H. Bluhm, Chem. Soc. Rev. **42**(13), 5833–5857 (2013).

[10] D. Llorens Rauret, A. Garzón Manjón, and J. Arbiol, Matter **8**(7), 102139 (2025).

[11] Y. Wu, J. Wang, X. Chen, J. C. Yang, and G. Zhou, J. Phys. Chem. Lett. **16**(25), 6570–6584 (2025).

[12] Y. Gu, Z. Qiu, S. Lin, Y. Han, H. Zhang, Z. Liu, and J. Cai, Rev. Sci. Instrum. **96**(6), 065203 (2025).

[13] Y. Han, H. Zhang, Y. Yu, and Z. Liu, ACS Catal. **11**(3), 1464–1484 (2021).

[14] C. M. Goodwin, P. Lömker, D. Degerman, B. Davies, M. Shipilin, F. Garcia-Martinez, S. Koroidov, J. Katja Mathiesen, R. Rameshan, G. L. S. Rodrigues, C. Schlueter, P. Amann, and A. Nilsson, Nature **625**(7994), 282–286 (2024).

[15] L. Sandoval-Diaz, D. Cruz, M. Vuijk, G. Ducci, M. Hävecker, W. Jiang, M. Plodinec, A. Hammud, D. Ivanov, T. Götsch, K. Reuter, R. Schlögl, C. Scheurer, A. Knop-Gericke, and T. Lunkenbein, Nat. Catal. **7**(2), 161–171 (2024).

[16] Q. Zhu, H. Zhou, L. Wang, L. Wang, C. Wang, H. Wang, W. Fang, M. He, Q. Wu, and F.-S. Xiao, Nat. Catal. **5**(11), 1030–1037 (2022).

[17] B. Qiao, A. Wang, X. Yang, L. F. Allard, Z. Jiang, Y. Cui, J. Liu, J. Li, and T. Zhang, Nat. Chem. **3**(8), 634–641 (2011).

[18] Y. Jiang, H. Li, Z. Wu, W. Ye, H. Zhang, Y. Wang, C. Sun, and Z. Zhang, Angew. Chem., Int. Ed. **55**(40), 12427–12430 (2016).

[19] B. L. Henke, E. M. Gullikson, and J. C. Davis, At. Data Nucl. Data Tables **54**(2), 181–342 (1993).

[20] H. Shinotsuka, S. Tanuma, C. J. Powell, and D. R. Penn, Surf. Interface Anal. **47**(9), 871–888 (2015).

[21] J. Cai, Y. Gu, Z. Wang, Y. Zang, S. Lin, T. Zhang, Y. Han, H. Zhang, Z.-J. Wang, and Z. Liu, Photon Sci. (to be published).

[22] P. Amann, D. Degerman, M.-T. Lee, J. D. Alexander, M. Shipilin, H.-Y. Wang, F. Cavalca, M. Weston, J. Gladh, M. Blom, M. Björkhage, P. Löfgren, C. Schlueter, P. Loemker, K. Ederer, W. Drube, H. Noei, J. Zehetner, H. Wentzel, J. Åhlund, and A. Nilsson, Rev. Sci. Instrum. **90**(10), 103102 (2019).

[23] R. S. Weatherup, B. Eren, Y. Hao, H. Bluhm, and M. B. Salmeron, J. Phys. Chem. Lett. **7**(9), 1622–1627 (2016).

[24] J. J. Velasco-Velez, V. Pfeifer, M. Hävecker, R. S. Weatherup, R. Arrigo, C.-H. Chuang, E. Stotz, G. Weinberg, M. Salmeron, R. Schlögl, and A. Knop-Gericke, Angew. Chem., Int. Ed. **54**(48), 14554–14558 (2015).

[25] A. Kolmakov, L. Gregoratti, M. Kiskinova, and S. Günther, Top. Catal. **59**(5–7), 448–468 (2016).

[26] L. J. Falling, R. V. Mom, L. E. Sandoval Diaz, S. Nakhaie, E. Stotz, D. Ivanov, M. Hävecker, T. Lunkenbein, A. Knop-Gericke, R. Schlögl, and J.-J. Velasco-Vélez, ACS Appl. Mater. Interfaces **12**(33), 37680–37692 (2020).

[27] F. Tao, L. Nguyen, M. Amati, and L. Gregoratti, Rev. Sci. Instrum. **95**(5), 055108 (2024).

[28] H.-Y. Chao, K. Venkatraman, S. Moniri, Y. Jiang, X. Tang, S. Dai, W. Gao, J. Miao, and M. Chi, Chem. Rev. **123**(13), 8347–8394 (2023).

[29] H. L. Xin, K. Niu, D. H. Alsem, and H. Zheng, Microsc. Microanal. **19**(6), 1558–1568 (2013).

[30] H. W. Kim, H. W. Yoon, S.-M. Yoon, B. M. Yoo, B. K. Ahn, Y. H. Cho, H. J. Shin, H. Yang, U. Paik, S. Kwon, J.-Y. Choi, and H. B. Park, Science **342**(6154), 91–95 (2013).

[31] S. K. Tiwari, S. Sahoo, N. Wang, and A. Huczko, J. Sci.: Adv. Mater. Devices **5**(1), 10–29 (2020).

[32] Z.-J. Wang, X. Kong, Y. Huang, J. Li, L. Bao, K. Cao, Y. Hu, J. Cai, L. Wang, H. Chen, Y. Wu, Y. Zhang, F. Pang, Z. Cheng, P. Babor, M. Kolibal, Z. Liu, Y. Chen, Q. Zhang, Y. Cui, K. Liu, H. Yang, X. Bao, H.-J. Gao, Z. Liu, W. Ji, F. Ding, and M.-G. Willinger, Nat. Mater. **23**(3), 331–338 (2024).

[33] J. Cai, Q. Dong, Y. Han, B.-H. Mao, H. Zhang, P. G. Karlsson, J. Åhlund, R.-Z. Tai, Y. Yu, and Z. Liu, Nucl. Sci. Tech. **30**(5), 81 (2019).

[34] R. Larciprete, S. Fabris, T. Sun, P. Lacovig, A. Baraldi, and S. Lizzit, J. Am. Chem. Soc. **133**(43), 17315–17321 (2011).

[35] X. Chen, J. Wang, S. B. Patel, S. Ye, Y. Wu, Z. Zhou, L. Qiao, Y. Wang, N. Marinkovic, M. Li, S. Hwang, D. N. Zakharov, L. Ma, Q. Wu, J. A. Boscoboinik, J. C. Yang, and G. Zhou, Nature **644**(8078), 927–932 (2025).

[36] M. C. Biesinger, B. P. Payne, L. W. M. Lau, A. Gerson, and R. S. C. Smart, Surf. Interface Anal. **41**(4), 324–332 (2009).

[37] D. Jennings, M. L. Weber, A. Meise, T. Binninger, C. J. Price, M. Kindelmann, I. Reimanis, H. Matsumoto, P. Cao, R. Dittmann, P. M. Kowalski, M. Heggen, O. Guillon, J. Mayer, F. Gunkel, and W. Rheinheimer, Nat. Commun. **16**(1), 6830 (2025).

[38] T.-S. Kim, J. Kim, H. C. Song, D. Kim, B. Jeong, J. Lee, J. W. Shin, R. Ryoo, and J. Y. Park, ACS Catal. **10**(18), 10459–10467 (2020).

[39] A. P. Lagrow, N. M. Alyami, D. C. Lloyd, O. M. Bakr, E. D. Boyes, and P. L. Gai, J. Microsc. **269**(2), 161–167 (2018).

[40] Y. Zhu and N. D. Browning, ChemCatChem **9**(18), 3478–3485 (2017).

[41] C. J. Powell, A. Jablonski, F. Salvat, and A. Y. Lee, NIST electron elastic-scattering cross-section database, version 4.0, 2016.

[42] M. Sun and Z.-J. Wang, Acc. Mater. Res. **6**(9), 1046–1051 (2025).